

The Aerosol Limb Imager: Acousto-Optic 2D Measurements of Limb Scattered Sunlight for Stratospheric Aerosol Profiling

Brenden J Elash, Adam E Bourassa, Paul R P Loewen, Douglas A Degenstein

August 24, 2015

Abstract

The Aerosol Limb Imager (ALI) is a remote sensing instrument designed to measure scattered sunlight from the atmospheric limb to retrieve spatially resolved information of the stratospheric aerosol distribution, including extinction coefficient and particle size. The long term goal of this work is the eventual realization of ALI on a satellite platform in low earth orbit. Here we present the development of an ALI prototype and the results from a test flight on a stratospheric balloon. The ALI instrument uses a large aperture Acousto-Optical Tunable Filter (AOTF) to image the stratospheric limb in a selectable narrow wavelength band ranging from the visible to the near infrared. The afocal optical system design uses telescopic front end optics to pass collimated light through the AOTF for each line-of-sight, which provides robust imaging that is relatively insensitive to impurities in the AOTF, at the cost of a small spectral gradient in the measured image that is negligible for the broad band aerosol spectral scattering characteristic. The ALI prototype was tested on a stratospheric balloon flight from the Canadian Space Agency (CSA) launch facility in Timmins, Canada, in September, 2014. Preliminary analysis of the hyperspectral images indicate that the radiance measurements are of high quality and have been used to retrieve vertical profiles of stratospheric aerosol extinction coefficient and one moment of the particle size distribution.

1 Introduction

Additional instruments with high resolutions on the order of 200 m vertically will satisfy the needs for current scientific investigation and will allow the determination of aerosol loading. Furthermore, there is a decrease in the number of satellites performing remote sensing of the atmosphere, newer instruments that fill the scientific requirements are required in order to replace these deficiencies. Stratospheric aerosol is one of these atmospheric constituents and plays a important role in the global radiative forcing balance (*Stocker et al.*, 2013). Causing

an overall cooling effect which is dependant on extinction and particle size distribution (*Kiehl and Briegleb*, 1993). Aerosol have been measured as for several decades though ground based instrumentation such as lidar (*Hamilton*, 1969). Studies have been preformed using ground based lidar to determine tropospheric aerosol loading (*Takamura et al.*, 1994; *Marenco et al.*, 1997; *Krueger et al.*, 1993). These ground based lidar measurements yields trends locally but lack global coverage. Similarity, balloon acquire excellent in-situ measurements with particle size and aerosol extinction (*Deshler et al.*, 2003) but also have only local coverage.

To increase the global coverage remote sensing initiatives were underwent and stratospheric aerosol has been monitored from satellite platforms throughout the last few decades. Solar occultation has provided a reliable, accurate and long term database of background and volcanic aerosol extinctions. Notable occultation instruments include SAM II (*McCormick et al.*, 1979), SAGE II (*McCormick*, 1987), and SAGE III (*Thomason and Taha*, 2003) and their combined life cycles gathered measurements from 1978 to 2005. These instruments compared well to ground based and airborne lidar measurements (*Russell and McCormick*, 1989). Although the method directly measures optical depth allowing for simple conversion to extinction without the need for particle size knowledge it is limited to 16 to 32 measurements per day since it requires a sunrise or sunset event.

A lidar has also been used on satellites to measure aerosol parameters with good vertical spatial resolution on the order of 10s of meters. CALIPSO (*Winker et al.*, 2007), a satellite lidar instrument, measures the atmosphere with profiles of 333 m horizontal resolution and 60 m, 180 m, and 300 m vertical resolution for the altitude ranges of 8.2-20.2 km, 20.2-30.1 km, and 30.1-40.0 km respectively. Although lidar instruments acquire global coverage they suffer from low signal to noise ratio which is especially problematic during the day limiting the ability to detect background aerosol levels (*Kacenelenbogen et al.*, 2011).

Another technique uses the limb scatter geometry, which measures scattered radiance from the sunlit atmosphere, and has been used to determine aerosol extinction. Although this geometry has the advantage of being able to measure the atmosphere throughout sunlit conditions with high signal to noise, the scattering process requires the use of a forward model to retrieve atmospheric parameters, making the inversion process from limb scatter measurements computationally heavy and time intensive. However, with the increase in computing power the computationally heavy retrievals can be readily preformed (*Bourassa et al.*, 2012). The Optical Spectrograph and InfraRed Imaging System (OSIRIS) a Canadian instrument onboard the Odin satellite (*Llewellyn et al.*, 2004) and SCanning Imaging Absorption spectroMeter for Atmospheric CHartographY (SCIAMACHY) onboard the ENVISAT (*Bovensmann et al.*, 1999) are two limb scatter instruments have successfully determined aerosol atmospheric parameters. These instruments are grating spectrometers with a single line of sight that acquire spectra at a single tangent altitude at a time so a series of exposures is required to create a vertical profile. With approximately a 1.5 km and 3 km vertical resolution for OSIRIS and SCIAMACHY respectively. Future instrumentations, like the Ozone Mapping Profiler Suite - Limb Profiler (OMPS-LP) (*Rault and Loughman*, 2013), image the the vertical limb to increase

the amount of data that can be acquired and increasing spatial along the track resolution.

The Atmospheric Limb Tracker for the Investigation of the Upcoming Stratosphere (ALTIUS) (*Dekemper et al.*, 2012) is a Belgium instrument designed by Belgian Institute for Space Aeronomy and its goal is to measure trace gas concentrations from measuring light in the limb scatter geometry as well as solar, stellar, and planetary occultation. ALTIUS is a multichannel instrument using three Acousto-Optic Tunable Filters (AOTF) with different wavelength bands. The three channels for ALTIUS are an ultraviolet, viable, and NIR with wavelength ranges of 250-450 nm, 450-900 nm, and 900-1800 nm respectively and each channel images the atmosphere with 2 spatial dimensions.

ALI is similar in concept to ALTIUS using the same novel filtering technology to address the much needed vertical resolution on the orders of hundreds of meters which is required to better understand aerosol transportation and climate effects. Furthermore, ALI will capture two dimensional images of the atmospheres allowing for better understanding of horizontal aerosol distributions and transportation. ALI will use the limb scatter geometry to gather 2-D spatial images of the atmosphere and gather spectral information by recording measurements at different wavelengths. AOTFs, ALI's spectral filter, operate efficiently in the Near InfraRed (NIR) which is a excellent wavelength range for sensitivity to aerosol signal (*Rieger et al.*, 2014). Inherently, AOTFs can only filter linear polarized light resulting in ALI only being able to measure a single polarization. The bandpass of the AOTF, approximately 2 nm at 600 nm and 7 nm at 1100 nm, are well suited with the broadband scattering characteristic of the aerosol signal. ALI measures scattered sunlight from 650-950 nm with a stratospheric balloon flight from Timmins Ontario in the fall of 2014.

2 Instrument Design

ALI is a simple imaging system that measures a single wavelength at a time through the use of an AOTF. The AOTF is a unique device that allows for the filtering of wavelengths without the use of any mechanical parts and has low power consumption. However, the AOTF requires consideration to account for its optical properties during the designing of the instrument. The AOTF causes a bend in the optical path of the measured signal and its diffractive qualities depend on the angle that the light enters the device. Furthermore the AOTF inherently only measures a specific polarization that will reduce the incoming radiance which must be accounted for in the design to achieve a high enough signal to noise ratio. As well, additional stray light is added to the system through the rejection of the other linear polarization which must be accounted for in the design.

2.1 Acousto-Optical Tunable Filter

The primary filtering device behind ALI and the technology that allows two dimensional spatial imaging is the AOTF. It uses an acoustic wave, with its wavelength being determined by a Radio Frequency (RF), that is propagated through the crystal and forms a standing wave to

create an effect similar to diffraction of a specific wavelength causing a filtering interaction. The use of an AOTF for an imaging system has several distinct advantages due to its low mass, fast stabilization times of a few microseconds, and no moving parts.

Large aperture, birefringent, non-collinear acousto devices are used in imaging systems and have been possible since the 1970s (*Chang, 1974*). A non-collinear device is where the input wave and acoustic wave are not aligned. Thanks to recent advancements of non-collinear AOTF technology these devices can be used efficiently in imaging systems (*Georgiev et al., 2002; Voloshinov et al., 2007*). To create the diffraction of a specific wavelength, a momentum matching criteria must be held where the wave vectors of the acoustic wave match the difference of the incoming and diffracted light wave vectors as seen in Figure 1. This condition is known as the Bragg matching criteria and is given by

$$\mathbf{k}_i = \boldsymbol{\kappa} + \mathbf{k}_d \quad (1)$$

where $|\mathbf{k}_i| = \frac{2\pi n_i}{\lambda}$ is the wave number of the incoming light, $|\mathbf{k}_d| = \frac{2\pi n_d}{\lambda}$ is the wave number of the diffracted light, and $|\boldsymbol{\kappa}| = \frac{2\pi F}{\nu}$ is the wave number of the acousto wave. The parameters λ , F , and ν are the wavelength in vacuum, the frequency of the RF wave, and the phase velocity in the crystal respectively. Using the condition given in Equation 1 and the wave vector diagram gives the following relation for a birefringent material undergoing Bragg diffraction

$$\lambda = \frac{\Delta n \nu}{F} \frac{\sin^2(\theta_i + \alpha)}{\sin \theta_i} \quad (2)$$

where Δn is the absolute difference between the ordinary and extraordinary indices of refraction, θ_i is the angle of incidence of the incoming light, and α is the angle the acoustic wave propagates through the device. This equation has several implications to the operation of the device which affects the design possibilities in an imaging system. First, the wavelength diffracted by the AOTF is inversely related to frequency of the RF wave. Second, the wavelength of diffracted signal is dependant on the angle of incidence of the incoming wave therefore passing a signal through the AOTF at different incident angles will result in different outgoing wavelengths. Also, through the described interaction, the diffracted light goes through a 90° rotation in polarization (*Voloshinov, 1996*).

A 10x10 mm aperture imaging quality ATOF was acquired from Brimrose of America. It is optically tuned, meaning designed for a specific wavelength octave, for a range of 600 to 1200 nm corresponding to a RF range of 156 to 70 MHz. It is made from tellurium dioxide (TeO₂), a birefringent crystal with indices of refraction at 800 nm of 2.226 and 2.373 for the ordinary and extraordinary modes respectively (*Uchida, 1971*). The extraordinary light is diffracted 2.7 degrees from the optical axis of the device. In order to achieve a constant diffraction angle the rear surface of the crystal is cut in a wedge shape to compensate for the angular change that occurs from altering the wavelength. The ordinary light undergoes diffraction but at a nonconstant angle from the optical axis with respect to wavelength. The AOTF diffraction can be seen in Figure 2. It is important to note that it is not possible

to have both polarizations compensated and ALI is designed to measure the extraordinary polarization.

2.2 Optical Design and Performance

The ALI prototype design and performance discussed in this work has been designed with balloon geometry in mind. For a stratospheric balloon at a float altitude of 35 km to be able to capture the a 35 km vertical and horizontal range a field of view of 6° is required.

Two possible designs were considered for ALI that met the optical requirements of the AOTF. Mainly, the incoming light must enter the device at less than the acceptance angle, which is the maximum angle light can enter the device and still undergo an efficient diffraction interaction. These two layouts are a telecentric and a telescopic system. The telescopic or afocal system causes a wavelength gradient to be formed across the field of view of the image whereas the telecentric design overcomes this problem but has a larger spectral point spread function (*Suhre et al.*, 2004). The optical design software Code V was used to assist in the designing of both of the optical layouts and was used to assist in choosing a final optical layout.

A telecentric layout on both the front and back end of the AOTF leads to focused light passing through the AOTF. The filtered image has a consistent wavelength across the entire image with a larger spectral point spread function since the diffracted wavelength is dependent on incident angle, as seen in Equation 2. This system does have two inherent issues. First, this method is sensitive to any surface defects of the crystal since the light enters the crystal in focused bundles. Second, a shift in the location of the imaging focal plane occurs that is dependant on wavelength and can only be corrected for a single wavelength. Defocusing will occur at the image plane for all other wavelengths and in order to correct for this problem additional compensating optics would need to be added or the CCD would need to be actively moved as the wavelengths are being scanned.

In the telescopic system the AOTF has collimated light for each line of sight passing through the device and this has a few fundamental changes that alter the system to both improve and degrade the imaging quality. First, the light passing through the AOTF from a single line of sight enters the AOTF at the same angle, so the image will have a narrower spectral PSF than the telecentric counterpart. However, each line of sight will be diffracted with a different fundamental central wavelength due to the angular dependance in the AOTF Bragg diffraction (Equation 2). The final image has a smaller spectral bandpass but there will be a wavelength gradient radiating out from the center of the image. Second, since light now passes through the AOTF collimated, the focal point of the image no longer changes with wavelength. Instead, a lateral displacement of each line of sight occurs based on the angle of incidence and the diffracted wavelength which causes a slight change in magnification of the final image. The lateral displacement that occurs is given by the following relation

$$\delta = (n(\lambda) - 1) \frac{t\theta}{n(\lambda)} \quad (3)$$

where δ is the displacement from the original path. This magnification is a negligible change overall amounting to a maximum 0.04 mm on the detector for the current ALI design.

Therefore, we have chosen a telescopic design. For ALI, a simple three lens optical layout was chosen for the system using Commercial Off-The-Shelf (COTS) components. Two lens before the AOTF form the front end optics and one lens behind comprises the back end optics. Before the light enters the AOTF, a linear polarizer with an extinction ratio of at least 100,000:1, is used to remove the incoming horizontal or ordinary polarized light, which is the polarization that is not imaged by ALI, removing the 0th and 1st order horizontal polarization from propagating through the system. The diffracted wavelength undergoes a 90° rotation in polarization so a second linear polarizer at 90° to the first is used after the AOTF to remove the undiffracted beam, see Figure 6. However a small percentage of the light is not absorbed by the polarizers causing an additional source of internal stray light. The diffracted light is 2.7° from the optical axis and to compensate, the rest of the optical chain after the AOTF is aligned with this direction. A final imaging lens forms the image of the signal on a QSI 616s CCD which has a 16 bit output with a 15 count error on the readout for typical operating temperatures. A ray tracing diagram for ALI's optical system was created using the CODE V optical design software and can be seen in Figure 5. Analysis of the final design was also performed using the CODE V optical design software to determine the minimum resolution required to achieve an MTF of 0.3 across the entire field of view. To achieve the minimum MTF desired across the entire field of view an average of 7 pixels is required making the average vertical and horizontal resolution of ALI across the entire field of view 210 m. The final optical specification for ALI can be found in Table 1. Due to contamination from the zeroth order beam, a loss of 1° horizontal field of view occurs on the right side of the field of view giving an effective field of view of 6° by 5° .

Effective focal length (mm)	74.3
Front optics magnification	0.67
Back optics magnification	1.27
Field of view ($^\circ$)	6.0 x 5.0
F-number	7.5
Image Size (mm)	9x7.5
Image Size (pixels)	1000x800
Resolved Image Size (averaged pixels)	143x114
Spectral Range (nm)	650-950

Table 1: ALI Final System Optical Parameters.

Another concern in the design of limb scatter instruments is the effect of out-of-field stray light that contaminates the final measurement. A front end baffle was designed and built using a method that minimizes the percentage of out-of-field light that will enter the entrance aperture without encountering at least three baffle surfaces before entering the aperture of ALI. To further reduce the unwanted signal, the baffle maintains a height to pitch ratio greater than

0.5 (*Fischer et al.*, 2008).

A SolidWorks rendition of the completed version of ALI can be seen in Figure 7. ALI is tilted at 3° from the horizontal so the complete 6° vertical field of view spans from the tangent point to the ground to the float altitude.

ALI is similar in concept to the Belgium instrument, ALTIUS, except ALTIUS uses a telecentric optical layout and is designed to measure atmospheric trace gases (*Dekemper et al.*, 2012). Trace gases have narrow absorption features that require higher spectral resolution. A telecentric layout will provide a constant wavelength across the whole field of view and is better suited for trace gases. The optical specifications are similar between the two instruments, however two key differences will be noted. First, by using a telescopic layout ALI's maximum field of view is determined by choosing lenses to ensure light enters ALI within the acceptance angle of the AOTF allowing for a larger possible field of view than on a telecentric system where the field view is defined by the aperture of the AOTF. Second, the $f/\#$ for ALTIUS is 14.32 compared to ALI's 7.5 which allows ALI to increase light throughput at the cost of slightly higher aberrations in the final image. The visible channel of ALTIUS was breadboarded and tested by imaging a smoke stack in order to determine NO_2 slant column density at 3.5 km away with a 10 second exposure times (*Dekemper et al.*, 2012). It was noted that improvements to the system would result from methods to reduce the amount of stray light that enters the ALTIUS system, as well as a reduction in the time in between measurements and an improvement in the flat-fielding and spectral calibrations of the instrument.

Software was designed for the ALI system to be used for the balloon campaign. ALI was operated with a Debian Linux operating system with threaded C++ based software to control the hardware and science operations that would initiate with system power on. The onboard computer was a VersaLogic PC-104 OCELOT computer with fanless operation and a 1.6 GHz Intel Atom processor with 2 GB of RAM and has a thermal operating range of -40 to 85°C . The onboard system communicated to a ground based station through UDP protocol and sends data, including images and house keeping information, to the ground, as well as receives commands from ground control.

3 Calibration

A series of calibrations were performed on ALI in order to characterize the system and was characterized in two stages. First the AOTF used in ALI was characterized to calibrate it with respect to wavelength and spectral sensitivity. Further, ALI was characterized as a complete system to be able to convert the measured data into radiances. The following calibration measurements were performed on ALI:

- AOTF wavelength calibration
- AOTF point spread function and diffraction efficiency
- Dark current and DC offset

- Stray light calibration
- Flat-fielding correction

3.1 AOTF Wavelength Calibration

The relationship between the applied RF and central diffracted wavelength was determined to know the accuracy and precision of the AOTF to select the centre wavelength. An experiment was set up to determine the wavelength dependance. In this experiment, linear polarizers were inserted before and after the AOTF to remove unwanted polarizations. 100 mm plano-convex lenses were chosen for the front and back end lenses to optimally fill the AOTF aperture. The light source was a 100 W quartz-tungsten halogen bulb that was collimated and passed into the first lens. The light passes through the AOTF focused then is re-collimated through the second lens. The signal enters a HORIBA iHR320 spectrometer with a spectral resolution of 1.175 nm which is below the factory specified resolution of the ATOF. The spectral results from the HORIBA spectrometer were imaged on a Synapse 354308 front-illuminated CCD detector with 1024x256 pixels. Images were taken at a constant exposure time at a set of RFs spaced every 150 kHz from 75 MHz to 160 MHz corresponding to nominally 1 nm resolution. The recorded spectrum was vertical and to increase signal to noise for each image the results are spectrally averaged across the rows and a typical result can be seen in Figure 3a. The maximum value of each image is taken to be the central wavelength through the AOTF at each respective RF.

The maximum values from each of the images were determined as well as the corresponding wavelengths for these values. It was noted that the wavelength versus RF curve (Figure 3c) was imperially noted to follow a power function of the form

$$F = a\lambda^b. \quad (4)$$

A linear least squares fit was performed in log space finding the coefficients a and b . The fit provided an agreement better than 0.6% within the testing range. A better fit was found in the form of

$$F = a\lambda^{b+c \log \lambda}. \quad (5)$$

These results can be seen in Figure 3c and Figure 3d. The agreement of this form is less than 0.1% throughout the whole wavelength range and the determined RF and wavelength relation as determined as

$$F = \exp(19.793)\lambda^{-3.381+0.168 \log \lambda} \quad (6)$$

where λ is in nanometers and F is in MHz with a 0.1% error in the central wavelength. It should be noted that even though the AOTF optical range is 600 nm to 1200 nm our analysis only measured wavelengths from 600 nm to 1080 nm due to the low quantum efficiency of the CCD beyond this range.

3.2 AOTF Point Spread Function and Diffraction Efficiency

The spectral point spread function and diffraction efficiency of the AOTF were determined to fully characterize the AOTF. The same set of data was used to determine the AOTF wavelength dependance was used to find the spectral point spread function by finding the Full Width Half Max for each wavelength. These results are shown in Figure 3b. The AOTF spectral resolution is well within the limits that are required in order to determine aerosol extinction in the upper troposphere and lower stratosphere since aerosol is a broadband scatterer.

The diffraction efficiency was determined using two sets of data; the first set is the data used to characterize the wavelength-RF dependance of the AOTF, the second set is a measurement of the light that was incident to the AOTF in the wavelength-RF dependance experiment. The second set, or incident set, of data, was acquired by removing the AOTF and posterior linear polarizer. The incident light source is measured with the HORIBA spectrometer with the same exposure time as the AOTF wavelength data set. By taking the ratio of the diffracted wavelength radiance over the incident radiance the diffraction efficiency was determined. The determined diffraction efficiency is between 56% to 64% across the measured spectral range and should be noted that the diffraction efficiency changes with respect to incoming angle (*Xu and Stroud, 1992*).

3.3 Dark Current and DC Offset

The DC offset is a bias that is applied to the analogue digital converter inside the CCD camera and needs to be removed in order to be able to get the pure measurement counts from the instrument. It is usually assumed that the DC offset for a CCD is a constant across the operating temperatures and exposure times of the device, however the DC offset for the camera used in ALI exhibited a temperature dependance. By using the dark images from the ascent of the flight, which was in darkness, combined with laboratory dark images all of which were recorded with the shortest possible exposure time of the camera, 0.01 s, to remove contribution from dark current. For all the images in the data set the mean value of the counts was used for DC offset determination. For each image the standard deviation of the counts ended up being 2 to 3 percent of the average value. Using this data, a curve was fit to determine the DC offset with respect to temperature and the curve is in the form of

$$\text{DC offset} = 0.00659T^3 - 0.09202T^2 - 3.5368T + 643.5127 \quad (7)$$

where T is the CCD temperature as measure from the CCD temperature sensor in degrees Celsius.

The dark current is the thermal energy that builds up in the CCD pixels that grows linearly with exposure time and temperature. The operating temperatures of ALI combined with the short exposure times lead to the system having a very small dark current contribution in the measurement images. The dark current was as small as a single count to at most seven counts for the worst case scenario (longest exposure time and hottest temperatures.) Since

this correction was small compared to the DC offset the dark current was added as a a noise contribution for the images.

3.4 Stray Light Calibration

An experiment to characterize the stray light of the overall system was performed. Two types of stray light exist; the first is out-of-field stray light is radiance that enters the optical path that is outside of the desired field of view. the second is internal stray light which is caused by optical elements not completely absorbing or removing any undesired wavelengths and polarizations. Stray light removal has always been a concern in atmospheric limb geometry instrumentation due to the difficulty in accurately discerning the signal in regards to the stray light contamination. Furthermore, ALI’s optical system has additional unwanted light internal stray light to the instrument because of the rejection of one of the polarizations due to the nature of the AOTF.

However, the diffraction interaction only occurs when the RF signal is applied, so without the RF wave the recorded measurement will only contain the stray light in the system. Using this characteristic, another experiment was devised to determine the stray light of the system. A 250 W quartz-tungsten light source was passed through a dispersing screen and into the entrance aperture of ALI filling the entire field of view. Using a variety of exposure times, ranging from 0.1 s to 60 s and wavelengths from 650 to 950 nm in 25 nm intervals, the incoming diffused light source was imaged twice; once with the AOTF in its off state, with no driving RF wave (Figure 8), and once with the ATOF in its on state, with the RF wave applied. For each pair of measurements the image with the “AOTF-off” only contains stray light in the system and the “AOTF on” image contains the stray light combined with the uniform signal from the light source. Subtracting the “AOTF-off” image from the “AOTF-on” image yields a final image that contains the desired signal. The resulting images were the brightest in the centre and experienced vignetting towards the edges. The vignetting is caused by the aperture of the AOTF. In order to be able to use this method during the balloon campaign all images captured will have a corresponding “AOTF-off” image, known as a calibration image, recorded as well.

3.5 Flat Fielding Correction

To complete calibrations, flat-fielding needs to be performed on the images to yield the radiances. The resulting images from the stray light removal experiment were used to determine the flat fielding corrections. The corrections were determined in two steps. First, the spatial corrections were determined for each wavelength and second, the spectral corrections were determined across wavelength. First for the spatial correction, for each wavelength, the mean value of the center 25 by 25 pixels of the images were used as the accepted value, and the determined mean value had approximately a 4% standard deviation. The spatial flat-fielding corrections were preformed by scaling each pixel to this average value with an associated 4%

error in the calibration.

Second, the spectral dependance was determined. ALI is most sensitive at 775 nm so this wavelength was chosen as the reference wavelength and all flat-fielding corrections were scaled to yield the same value as the 775 nm spatially flat fielded images. The choice to relatively calibrate the ALI radiances to the 775 nm value was performed since no absolute calibration was performed on ALI. The final flat-fielding corrections were the combination of the spatial and spectral corrections. The final images radiances are called relative radiance since the results are not absolutely calibrated.

4 Stratospheric Balloon Flight

4.1 Flight Day Conditions and Flight Path

The CSA balloon launch base is in Timmins, Ontario (48.47°N 81.33°W). ALI was integrated onto the CNES CARMEN-2 gondola with CARMEN-2's systems, including communications and power. CARMEN-2 is a pointed gondola and its pointing precision is better than 1' with the use of an onboard star tracker. ALI was orientated so it would be 90° from the azimuthal direction of the sun with an overall southern field of view during the mission. ALI measures light that is polarized vertically and computed values shows the vertical polarization only accounts for 10 to 35% of the total incoming radiance for the balloon geometry and is sufficient signal for ALI to measure.

On September 20, 2014 at 05:35 UTC (01:35 local time) ALI was launched as part of the Nimbus 7 mission from the CSA Timmins balloon launch facility. During the launch, the sky was clear with light winds allowing for a safe and uneventful launch. The ascent of CARMEN-2 occurred in darkness and reached its flight altitude of 36.5 km at 8:17 UTC. First light was observed by ALI at 9:39 UTC and recorded measurements until 14:42 UTC when the primary aerosol observations were complete and ALI was powered off at 17:15 UTC. A visualization of the flight path with major landmarks noted can be found on Figure 9a. Temperature profiles for the ambient atmosphere and instrument can be seen in Figure 9b. The black curve is the ambient atmospheric temperature surrounding the gondola during the flight from the ECMWF (*Molteni et al.*, 1996). ALI was thermally insulated with foam to keep the system warm, while at the same time direct heating from the sun was a concern so the system was covered in a reflecting material to reduce solar heating.

During the mission, ALI operated in two primary acquisition modes, a calibration mode and an aerosol imaging mode. The first mode, the calibration mode, was primarily used during ascent when the gondola was in the darkness and intermittently between aerosol modes during sunlit conditions. During this mode the filtering of the AOTF was disabled and the system images dark current and DC offset during the ascent and stray light during the sunlit conditions. Eight exposures are taken in the calibration mode with 0.05, 0.1, 0.5, 1, 2, 3, 5, 10 second exposure times. The second operational mode, the aerosol mode, recorded measurements in a measurement cycle and each measurement cycle contained 13 measurement sets and each

measurement set contains two images, a calibration image and a measurement image. Each measurement set was recorded at wavelengths at every 25 nm between 650 to 950 nm. Each measurement cycle took approximately 10 minutes to run with each measurement set taking approximately 45 seconds to acquire with exposure time for images varying between 0.5 to 6 seconds.

4.2 Measurements

After the successful recovery of ALI, 216 raw images were download (known as the level 0 data) and calibration was performed to convert them into relative radiances (level 1 data). Using the calibrations from section 3, the images were converted to relative radiances. An example of an image with all calibrations applied can be seen in Figure 10a. This is image number 212 at 750 nm taken at 13:57 UTC with a solar zenith angle and solar scattering angle of 63° and 98° respectively.

To increase the precision of the measurements to a minimum of 0.3 MTF from the flight the images were averaged in cells of 25 horizontal pixels and vertical pixels were averaged to be on a 1 km grid. ALI radiance profiles from the complete mission from the center column of the detector are shown in Figure 11. The first set of radiance profiles, the dashed lines, that start near zero and move toward the large values are the radiance profiles that were recorded during sunrise when the solar zenith angle was greater than 90° and the gradual increase was therefore expected. Once the sun had completely risen, where solar zenith angle is less than 90° represented by the solid lines, the relative radiance vectors follow a similar shape and have a similar magnitude with some variability corresponding largely to thin clouds. These thin clouds were observed from the ground during the mission and were formed after the sunrise. Image 212 was selected to demonstrate radiance differences between different horizontal lines of sight which can be seen in Figure 10b. The anomaly is determined by calculating the mean vertical relative radiance profile and removing it across the field of view. These clouds appeared to have a maximum height of two kilometers. It should also be noted that some high altitude stray light appears in the final image from an unknown source. Lastly, images 204 to 216 were used to show the spectrum of relative radiances at a series of altitudes which is seen in Figure 12 with the error of the relative radiances represented by the shading. These relative radiances were compared to calculated values with a background atmosphere and the two sets of data were similar in radiance fall out.

4.3 Retrievals

The modeled radiances for the nonlinear inversion were computed with the SASKTRAN radiative transfer engine (*Bourassa et al.*, 2008a) for High Resolution (SASKTRAN-HR) (*Zawada et al.*, 2015) measurements using the newly developed polarization module (*Dueck S. and De-genstein*). The polarized output of SASKTRAN-HR gives the Stokes vectors for the radiance on the model reference frame which can then be rotated into the instrument's coordinate sys-

tem. Once rotated the polarization required to match the ALI measurement is the vertical polarization given by

$$I_v = \frac{1}{2} (I - Q) \quad (8)$$

where I and Q are Stokes parameters defined by $I = \langle E_x^2 \rangle + \langle E_y^2 \rangle$ and $Q = \langle E_x^2 \rangle - \langle E_y^2 \rangle$. The variables E_x and E_y are the horizontal and vertical component of the electric field in the instrument frame.

The relative radiances from ALI are used to create measurement vectors, \mathbf{y} , following from *Bourassa et al.* (2012) in the following form

$$\mathbf{y} = \log \left(\frac{\mathbf{I}_v(\mathbf{z}, \lambda)}{I_v(z_{ref}, \lambda)} \right) - \log \left(\frac{\mathbf{I}_{v,rayleigh}(\mathbf{z}, \lambda)}{I_{v,rayleigh}(z_{ref}, \lambda)} \right) \quad (9)$$

where $\mathbf{I}_v(\mathbf{z}, \lambda)$ is the measured radiance from ALI and $I_v(z_{ref}, \lambda)$ is the radiance at a reference altitude used to normalize the signal from a high altitude where there is little aerosol contribution. For ALI the highest possible altitude where the signal is above the noise threshold is approximately 30 km tangent height. The second term uses modeled radiances from SASKTRAN-HR with only the molecular atmosphere to approximately remove the Rayleigh signal. This is done to improve the speed of the convergence of the retrieval. An initial guess state, \mathbf{x} , for the aerosol extinction and particle size distribution profiles are set in the SASKTRAN-HR model. The forward model vector is constructed similarly to the measurement vector. It is used in combination with the measurement vector to update the extinction profile using Multiplicative Algebraic Reconstruction Technique (MART) algorithm which was developed for use in the OSIRIS retrievals (*Bourassa et al.*, 2012) with the following iterative technique

$$x_i^{n+1} = x_i^n \sum_j \frac{y_j}{F(z_j)} W_{ij} \quad (10)$$

where x_i is the aerosol extinction at each shell altitude, i and j is the tangent point from the measurements. W_{ij} is the weighting matrix that relates the importance of each measurement vector to each shell altitude. This method was outlined by *Bourassa et al.* (2007) and allows for fast retrievals without calculating a Jacobian which can be computationally expensive for limb scatter.

Once a retrieval has been completed for an image the result is used to estimate the error in the returned extinction. For each altitude, a gain matrix, \mathbf{G} , is created by perturbing the retrieved profile. The error at each retrieved altitude is then given by

$$\mathbf{E} = \mathbf{G} \mathbf{S}_e \mathbf{G}^T \quad (11)$$

where \mathbf{S}_e is the covariance matrix of the measurement vector and \mathbf{E} is the covariance of the retrieved aerosol profile (*Rodgers*, 2000). The precision for ALI is the square root of the diagonal of \mathbf{E} .

Once the retrieval has been performed for a complete series of wavelengths; determination

of the Angström exponent is performed in a similar method as outlined by *Rault and Loughman* (2013) for the OMPS aerosol particle size retrieval. From Equation 12, the particle size profile from a series wavelength can be determined from the Angström exponent. We assume the the measurements observe the same atmosphere during one complete measurement cycle; the differences between extinction ratios at the different wavelength can be used to gather a understanding of aerosol particle size in the form

$$\frac{n\sigma}{n_0\sigma_0} = \left(\frac{\lambda}{\lambda_0}\right)^{-\alpha} \quad (12)$$

which characterizes the cross section particle size dependance verses wavelength where n is the aerosol concentration, and σ is the scattering cross section. For the retrieval described here a single mode log-normal distribution is assumed with a mode radius, r_g , and the mode width, σ_g , which is the same as the OSIRIS version 5.07 aerosol product. At each retrieved altitude the extinction from each wavelength is used to fit the Angström exponent. Then the median value from all the retrieved altitudes is used as the new size parameters in next iteration of the retrieval. The mode width is set at a constant 1.6 and the mode radius is allowed to vary to match the Angström exponent retrieved (*Bourassa et al.*, 2008b; *Rieger et al.*, 2014). The mode radius is updated and the process is repeated, re-retrieving the extinction profiles, until the Angström exponent converges. At the end of the last iteration, the Angström exponent profile is reported as the final particle size product.

In order to be able to use the ALI data in the MART method, atmospheric inputs were needed for the model; albedo, ozone concentration and cross sections, and aerosol cross sections. The ozone absorbtion features from the Chappuis band appear in the ALI measurements from 650 to 700 nm and suitable ozone profiles were required to correction. Ozone profiles from OSIRIS were chosen since the instrument has compared well to other ozone measuring instruments (*Bourassa et al.*, 2014) and five profiles existed that were within 48 hours of the balloon flight and within 500 km of the launch facility and were averaged together to be the ozone profile used in the SASKTRAN-HR model, with cross sections from *Burrows et al.* (1999). The albedo is from the ADAM database (*Muller et al.*, 2013) which has monthly values for albedo over the surface on earth at a resolution of $0.1^\circ \times 0.1^\circ$ grid at 1 nm spectral resolution. The aerosol cross sections come from the Mie scattering derivation that was originally proposed by Mie and was implemented efficiently by *Wiscombe* (1980). For the purpose of the retrieval an initial guess profile was used with a constant mode radius of 0.08 μm and a mode width of 1.6 which is considered a standard size distribution for aerosol (*Deshler et al.*, 2003).

4.4 Results

The complete mission consisted of 216 images that were recorded in illuminated conditions. The MART retrieval method was run on a select set for the purpose of the analysis, specifically the last complete set of images from 650 to 950 nm consisting of images 204-216. The complete set of retrieved aerosol extinction profiles can be seen in the left panel of Figure 13. After

the retrieval, the difference between the measurement and forward model vectors were less than 2% for the majority of the retrieval region, approximately 13 km to 24 km, across all wavelengths. From the retrieval altitudes, the aerosol extinction shows a decrease as the wavelength increases which is expected due to the dependance of the cross section with respect to particle size.

The aerosol profile for the ALI 750 nm aerosol extinction is shown in blue with the shading representing the precision of the retrieved profile on the right of Figure 13. The error is strictly based on measurement error and neglects any model and atmospheric state errors. The green curve is the average 750 nm aerosol extinction profiles of the same five OSIRIS scans used for the ozone profile and red is the 750 nm aerosol extinction from SALOMON (*Berthet et al.*, 2002) which was launched from the Timmins balloon base as the Nimbus 5 mission on September 12, 2014. The aerosol extinction for ALI and OSIRIS are within 50% of each other for a majority of the 750 nm profile and is the wavelength where agreement is best. The ALI profiles does not account for modeling systematics so the difference is acceptable. It also should be noted that the three instruments follow the same overall profile shape. First, a bend in the profile occurs at approximately 25 km, then increases approximately linearly until 15 km where aerosol extinction leaves the linear trend and forms the peak of the measurement.

The particle size method was used as outlined in the pervious section. The first panel of Figure 14 shows the median Angström exponent that was determined after each iteration and convergence can be seen after a couple iterations. The particle size determined for ALI in the last complete set of aerosol images can be seen in the second panel of Figure 14 which yields a final Angström exponent of between 2 and 3 throughout the altitude range from 13 to 22 km. Assuming a mode width of 1.6 yields a median mode radius of 0.096 μm .

In order to determine the Angström exponent a least squares fit was used on the extinctions for all wavelengths at each altitude. An extinction at an altitude was rejected from the fit if the forward model at that shell altitude was not within 2% of the measurement vector. In the case shown in Figure 14, the 20.5 km shell altitude, only 10 of the 13 possible wavelengths contributed to the determination of the Angström exponent.

ALI successfully determined stratospheric aerosol profiles during the Timmins campaign and is considered a success. Aerosol profiles were determined from the ALI data and no large scale issues were noted with the instrument; however, some future changes would be recommended that would allow ALI to better measure aerosol profiles. First, an absolute calibration of the instrument would allow ALI to determined its own albedo, removing some the uncertainly in the model inputs which would yield higher quality measurements. Second, a measurement set took on average 45 s to finish but most exposure times were less than 5 s in total. Most of time was spent reading the data off of the camera. A future iteration of ALI should be equipped with a camera that allows the data quickly read to increase the data output. Third, a thermal study of the optics for flight temperatures would possibly allow for higher resolution measurements and retrievals to be achieved. Optical changes due to temperature were not known and may have led to resolution losses. Fourth, even with the

robust method of removing stray light with the functionality of the AOTF, some stray light was still noticed on the final images and improvement to the reduction of this contamination would help increase measurement quality even further. And lastly, capturing a calibration image for every measurement image was not necessary. The stray light between several images in a row does not greatly change and the number of calibration images could be reduced in a future mission increases data output.

However, the data from ALI overall was of good quality. A future satellite mission with a ALI type design would be able to image the atmosphere with good global coverage and resolution. ALI would be a good supplement to occultation, lidar, nadir, limb scatter, and in situ measurements to further monitor the earth’s aerosol extinction level and climate change.

5 Conclusions

A description of the ALI prototype using an AOTF for active filtering in the visible to near IR with a telescopic optical layout with the purpose to measure aerosol extinction from the upper troposphere and lower stratosphere with a high vertical and horizontal resolution with images was presented here. The AOTF has fast stabilization times and the ability to disable the filter gives an excellent method to remove stray light from the final measurements.

ALI was tested on board the CARMEN-2 gondola from the balloon launch facility at Timmins, Ontario. Aerosol extinction profiles were determined and had good comparisons to OSIRIS and SALOMON in profile shape. The absolute extinction values are different by a large amounts but can be attributed to the large amount of unaccounted systematics in the retrieval algorithm. Overall, ALI performed admirably and verified the use of this technology for future atmospheric remote sensing missions.

Future upgrades to ALI would include the realignment of the optics for flight temperatures to allow for higher resolution measurements and retrievals. Another improvement would be replacing the CCD currently used on ALI with a camera with faster readout would allow for a higher quantity of data to be taken by reducing the approximate 45 s readout time down to a smaller value necessary for a satellite missions on the order of 1 s per wavelength.

6 Acknowledgements

This work would have not been possible without funding from the CSA to design and build ALI through the FAST program as well as the CSA building and managing the launch facility in Timmins, Ontario. Also, thanks to CNES for funding and overseeing the launches at Timmins in 2014. As well, thanks to Nick Lloyd for help in development of the flight code, without his efforts this work would have not been accomplished.

References

- Berthet, G., J.-B. Renard, C. Brogniez, C. Robert, M. Chartier, and M. Pirre (2002), Optical and physical properties of stratospheric aerosols from balloon measurements in the visible and near-infrared domains. i. analysis of aerosol extinction spectra from the amon and salomon balloonborne spectrometers, *Applied optics*, *41*, 7522–7539.
- Bourassa, A. E., D. A. Degenstein, R. L. Gattinger, and E. J. Llewellyn (2007), Stratospheric aerosol retrieval with optical spectrograph and infrared imaging system limb scatter measurements, *Journal of Geophysical Research (Atmospheres)*, *112*, D10217, doi:10.1029/2006JD008079.
- Bourassa, A. E., D. A. Degenstein, and E. J. Llewellyn (2008a), SASKTRAN: A spherical geometry radiative transfer code for efficient estimation of limb scattered sunlight, *Journal of Quantitative Spectroscopy and Radiative Transfer*, *109*, 52–73, doi:10.1016/j.jqsrt.2007.07.007.
- Bourassa, A. E., D. A. Degenstein, and E. J. Llewellyn (2008b), Retrieval of stratospheric aerosol size information from OSIRIS limb scattered sunlight spectra, *Atmospheric Chemistry & Physics*, *8*, 6375–6380.
- Bourassa, A. E., L. A. Rieger, N. D. Lloyd, and D. A. Degenstein (2012), Odin-OSIRIS stratospheric aerosol data product and SAGE III intercomparison, *Atmospheric Chemistry & Physics*, *12*, 605–614, doi:10.5194/acp-12-605-2012.
- Bourassa, A. E., D. A. Degenstein, W. J. Randel, J. M. Zawodny, E. Kyrölä, C. A. McLinden, C. E. Sioris, and C. Z. Roth (2014), Trends in stratospheric ozone derived from merged sage ii and odin-osiris satellite observations, *Atmospheric Chemistry and Physics*, *14*, 6983–6994, doi:10.5194/acp-14-6983-2014.
- Bovensmann, H., J. Burrows, M. Buchwitz, J. Frerick, S. Noël, V. Rozanov, K. Chance, and A. Goede (1999), Sciamachy: Mission objectives and measurement modes, *Journal of the Atmospheric Sciences*, *56*, 127–150.
- Burrows, J., A. Richter, A. Dehn, B. Deters, S. Himmelman, S. Voigt, and J. Orphal (1999), Atmospheric remote-sensing reference data from gome2. temperature-dependent absorption cross sections of o₃ in the 231–794nm range, *Journal of Quantitative Spectroscopy and Radiative Transfer*, *61*, 509–517.
- Chang, I. C. (1974), Noncollinear acousto-optic filter with large angular aperture, *Applied Physics Letters*, *25*, 370, doi:10.1063/1.1655512.
- Dekemper, E., N. Loodts, B. V. Opstal, J. Maes, F. Vanhellemont, N. Mateshvili, G. Franssens, D. Pieroux, C. Bingen, C. Robert, L. D. Vos, L. Aballea, and D. Fussen (2012), Tunable

- acousto-optic spectral imager for atmospheric composition measurements in the visible spectral domain, *Applied Optics*, *51*, 6259–6267, doi:10.1364/AO.51.006259.
- Deshler, T., M. Hervig, D. Hofmann, J. Rosen, and J. Liley (2003), Thirty years of in situ stratospheric aerosol size distribution measurements from laramie, wyoming (41 n), using balloon-borne instruments, *Journal of Geophysical Research: Atmospheres (1984–2012)*, *108*.
- Dueck S., A. E., Bourassa, and D. A. Degenstein (), SASKTRAN-HR Polarization Module, *In Preparations*.
- Fischer, H., M. Birk, C. Blom, B. Carli, M. Carlotti, T. v. Clarmann, L. Delbouille, A. Dudhia, D. Ehnhalt, M. Endemann, et al. (2008), Mipas: an instrument for atmospheric and climate research, *Atmospheric Chemistry and Physics*, *8*, 2151–2188.
- Georgiev, G., D. A. Glenar, and J. J. Hillman (2002), Spectral characterization of acousto-optic filters used in imaging spectroscopy, *Appl. Opt.*, *41*, 209–217, doi:10.1364/AO.41.000209.
- Hamilton, P. (1969), Lidar measurement of backscatter and attenuation of atmospheric aerosol, *Atmospheric Environment (1967)*, *3*, 221–223.
- Kacenelenbogen, M., M. Vaughan, J. Redemann, R. Hoff, R. Rogers, R. Ferrare, P. Russell, C. Hostetler, J. Hair, and B. Holben (2011), An accuracy assessment of the caliop/calipso version 2/version 3 daytime aerosol extinction product based on a detailed multi-sensor, multi-platform case study.
- Kiehl, J. T., and B. P. Briegleb (1993), The relative roles of sulfate aerosols and greenhouse gases in climate forcing, *Science*, *260*, 311–314, doi:10.1126/science.260.5106.311.
- Krueger, D., L. Caldwell, C. She, and R. Alvarez (1993), Self-consistent method for determining vertical profiles of aerosol and atmospheric properties using a high spectral resolution rayleigh-mie lidar, *Journal of Atmospheric and Oceanic Technology*, *10*, 533–545.
- Llewellyn, E., N. D. Lloyd, D. A. Degenstein, R. L. Gattinger, S. V. Petelina, A. E. Bourassa, J. T. Wiensz, E. V. Ivanov, I. C. McDade, B. H. Solheim, J. C. McConnell, C. S. Haley, C. von Savigny, C. E. Sioris, C. A. McLinden, E. Griffioen, J. Kaminski, W. F. J. Evans, E. Puckrin, K. Strong, V. Wehrle, R. H. Hum, D. J. W. Kendall, J. Matsushita, D. P. Murtagh, S. Brohede, J. Stegman, G. Witt, G. Barnes, W. F. Payne, L. Piche, K. Smith, G. Warshaw, D. L. Deslauniers, P. Marchand, E. H. Richardson, R. A. King, I. Wevers, W. McCreath, E. Kyrola, L. Oikarinen, G. W. Leppelmeier, H. Auvinen, G. Megie, A. Hauchecorne, F. Lefevre, J. de La Noe, P. Ricaud, U. Frisk, F. Sjoberg, F. von Scheele, and L. Nordh (2004), The OSIRIS instrument on the Odin spacecraft, *Canadian Journal of Physics*, *82*, 411–422, doi:10.1139/p04-005.

- Marenco, F., V. Santacesaria, A. F. Bais, D. Balis, A. di Sarra, A. Papayannis, and C. Zerefos (1997), Optical properties of tropospheric aerosols determined by lidar and spectrophotometric measurements (photochemical activity and solar ultraviolet radiation campaign), *Applied Optics*, *36*, 6875–6886.
- McCormick, M. (1987), Sage ii: an overview, *Advances in space research*, *7*, 219–226.
- McCormick, M., P. Hamill, W. Chu, T. Swissler, L. McMaster, and T. Pepin (1979), Satellite studies of the stratospheric aerosol, *Bulletin of the American meteorological Society*, *60*, 1038–1046.
- Molteni, F., R. Buizza, T. N. Palmer, and T. Petroligis (1996), The ecmwf ensemble prediction system: Methodology and validation, *Quarterly Journal of the Royal Meteorological Society*, *122*, 73–119.
- Muller, J.-P., P. Lewis, F.-M. Bréon, C. Bacour, I. Price, L. Chaumat, P. Prunet, L. Gonzales, C. Schlundt, M. Vountas, et al. (2013), A surface reflectance database for esas earth observation missions (adam), *Living Planet Symposium*.
- Rault, D. F., and R. P. Loughman (2013), The omps limb profiler environmental data record algorithm theoretical basis document and expected performance, *Geoscience and Remote Sensing, IEEE Transactions on*, *51*, 2505–2527.
- Rieger, L. A., A. E. Bourassa, and D. A. Degenstein (2014), Stratospheric aerosol particle size information in odin-osiris limb scatter spectra, *Atmospheric Measurement Techniques*, *7*, 507–522, doi:10.5194/amt-7-507-2014.
- Rodgers, C. (2000), *Inverse Methods for Atmospheric Sounding: Theory and Practice*, Series on atmospheric, oceanic and planetary physics: 1999, World Scientific.
- Russell, P., and M. McCormick (1989), Sage ii aerosol data validation and initial data use: An introduction and overview, *Journal of Geophysical Research: Atmospheres (1984–2012)*, *94*, 8335–8338.
- Stocker, T. F., D. Qin, G.-K. Plattner, M. M. Tignor, S. K. Allen, J. Boschung, A. Nauels, Y. Xia, V. Bex, and P. M. Midgley (2013), *Climate Change 2013 The Physical Science Basis*.
- Suhre, D. R., L. J. Denes, and N. Gupta (2004), Telecentric confocal optics for aberration correction of acousto-optic tunable filters, *Applied Optics*, *43*, 1255–1260, doi:10.1364/AO.43.001255.
- Takamura, T., Y. Sasano, and T. Hayasaka (1994), Tropospheric aerosol optical properties derived from lidar, sun photometer, and optical particle counter measurements, *Applied Optics*, *33*, 7132–7140.

- Thomason, L. W., and G. Taha (2003), Sage iii aerosol extinction measurements: Initial results, *Geophysical research letters*, 30.
- Uchida, N. (1971), Optical properties of single-crystal paratellurite (TeO_2), *Phys. Rev. B*, 4, 3736–3745, doi:10.1103/PhysRevB.4.3736.
- Voloshinov, V. (1996), Spectral and polarization analysis of optical images by means of acousto-optics, *Optics Laser Technology*, 28, 119–127, doi:10.1016/0030-3992(95)00079-8.
- Voloshinov, V. B., K. B. Yushkov, and B. B. J. Linde (2007), Improvement in performance of a TeO_2 acousto-optic imaging spectrometer, *Journal of Optics A: Pure and Applied Optics*, 9, 341–347, doi:10.1088/1464-4258/9/4/006.
- Winker, D. M., W. H. Hunt, and M. J. McGill (2007), Initial performance assessment of caliop, *Geophysical Research Letters*, 34.
- Wiscombe, W. J. (1980), Improved mie scattering algorithms, *Applied optics*, 19, 1505–1509.
- Xu, J., and R. Stroud (1992), *Acousto-optic devices: principles, design, and applications*, vol. 12, Wiley-Interscience.
- Zawada, D. J., S. R. Dueck, L. A. Rieger, A. E. Bourassa, N. D. Lloyd, and D. A. Degenstein (2015), High resolution and monte carlo additions to the sasktran radiative transfer model, *Atmospheric Measurement Techniques Discussions*, 8, 3357–3397, doi: 10.5194/amtd-8-3357-2015.

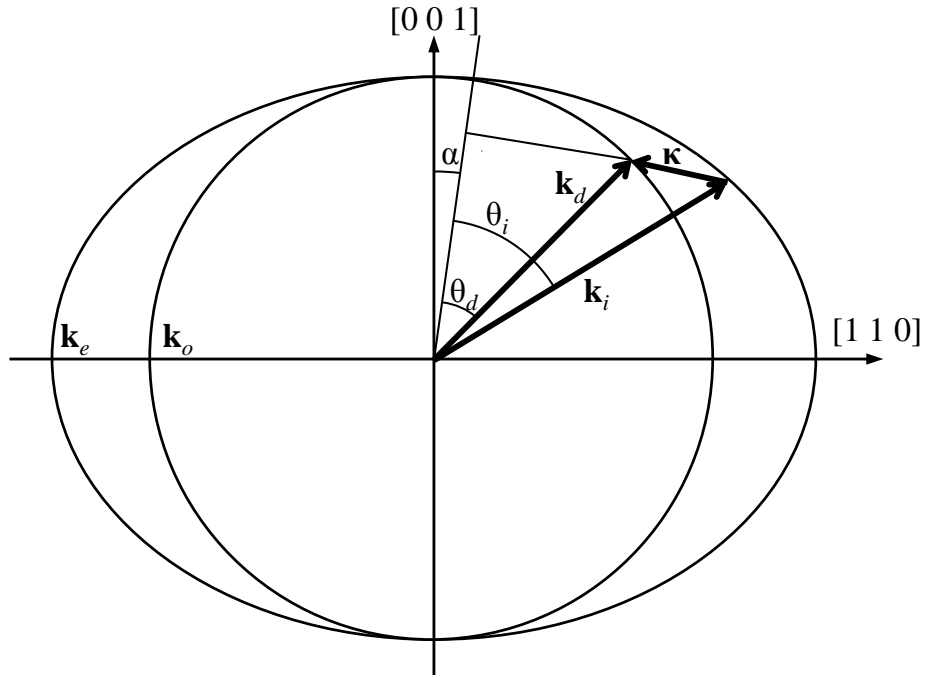


Figure 1: The wave vectors generated by the AOTF experiment. From Equation 1, the incident wave vector, \mathbf{k}_i , diffracted wave vector, \mathbf{k}_d , and acoustic wave vector $\boldsymbol{\kappa}$ are shown. The respective interaction angles for the incident and diffracted wave vectors θ_i and θ_d are also presented.

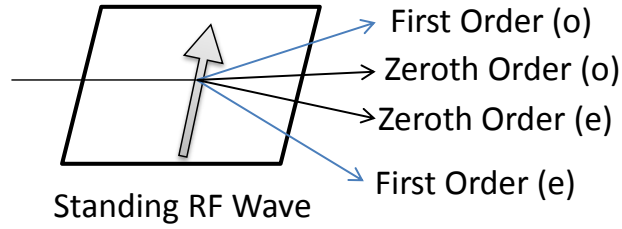


Figure 2: An AOTF undergoing Bragg diffraction with an unpolarized input with a RF wave applied represented by the arrow. After the diffraction event four output signals are formed: the zeroth order and first order ordinary and extraordinary signals. However the only optical path that remains at a constant angle no matter the applied RF wavelength is the first order extraordinary diffracted signal.

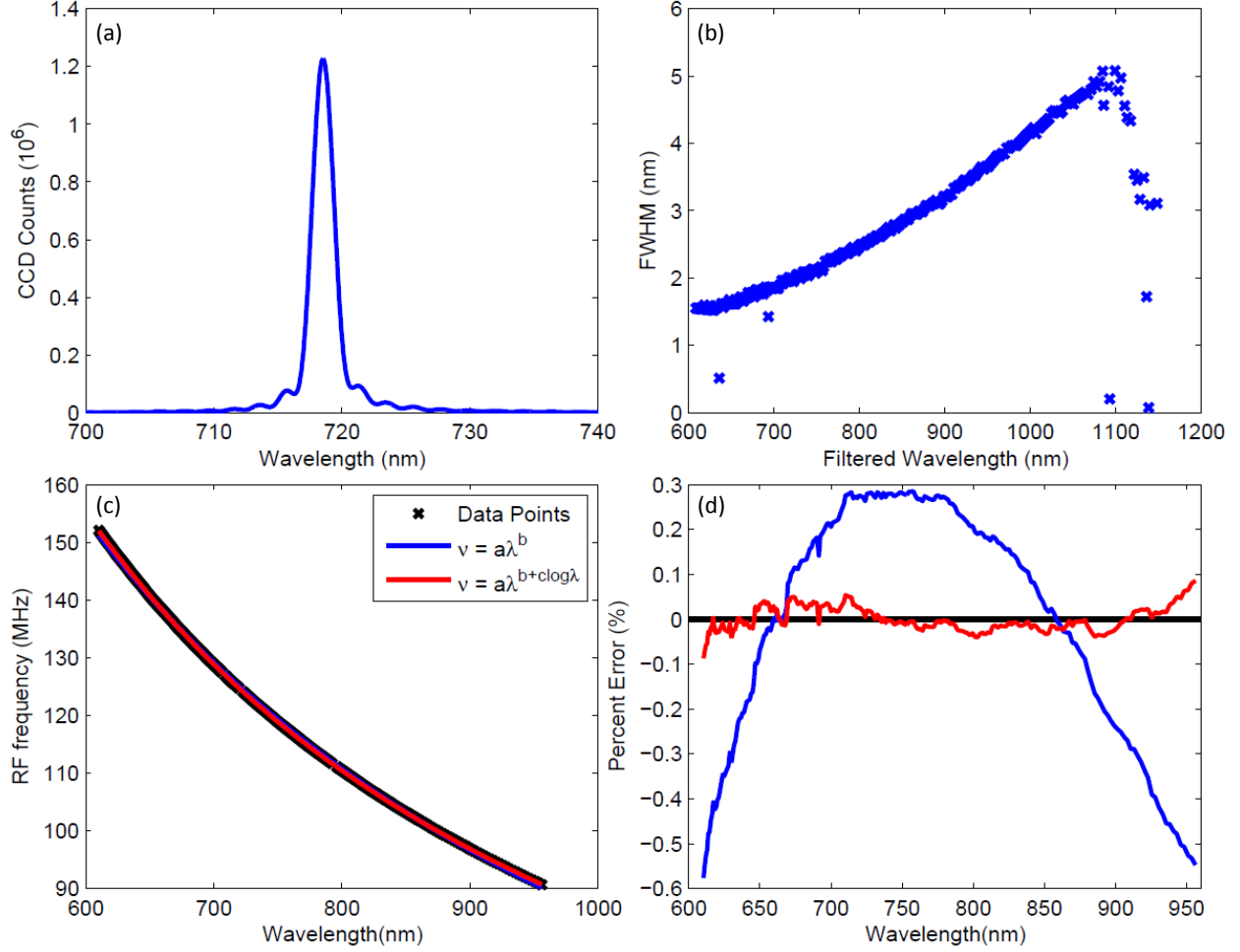


Figure 3: (a) A row averaged image taken from the AOTF calibration experiment when the tuning frequency of the AOTF was at 124.96 MHz. (b) The FWHM for each of the determined wavelengths for the AOTF. The FWHM at 600 nm is 1.5 and as the wavelengths get longer the FWHM increases to 4.9 at 1080 nm. (c) The calibration curves for the AOTF RF versus the diffracted wavelength which contains the data points recorded and two best fit curves. (d) The percent error with respect to the measured frequency for the two best fit curves in the previous panel.

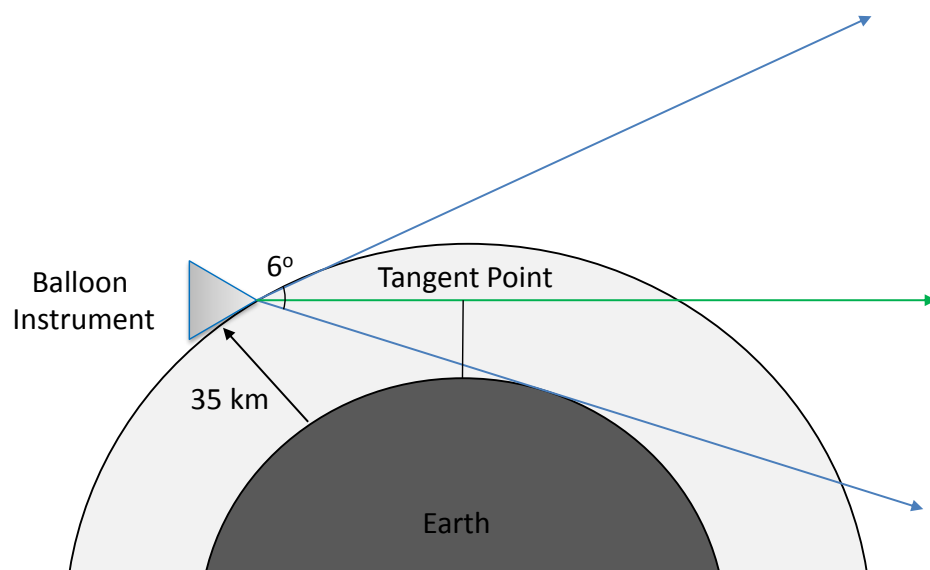


Figure 4: ALI in a stratospheric balloon geometry showing the complete 6° field of view in blue with a float altitude of 35 km. The green shows a typical vertical line of sight where the tangent point or altitude is set by the minimum distance between the earth and the line of sight.

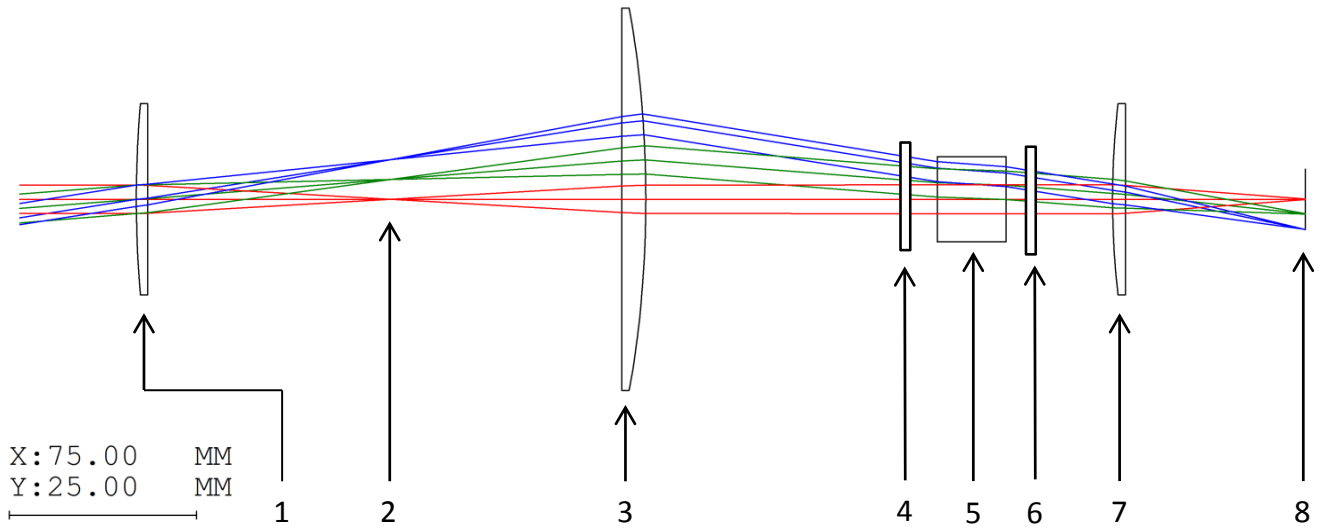


Figure 5: Ray Tracing diagram of the telescopic lens system for ALI simulated by Code V optical design software. The elements in the system are the following: (1) 150 mm focal length plano-convex lens. (2) Slit plate. (3) 100 mm focal length plano-convex lens. (4) Vertical linear polarizer. (5) Brimrose AOTF. (6) Horizontal linear polarizer. (7) 50.4 mm focal length plano-convex lens. (8) Imaging plane.

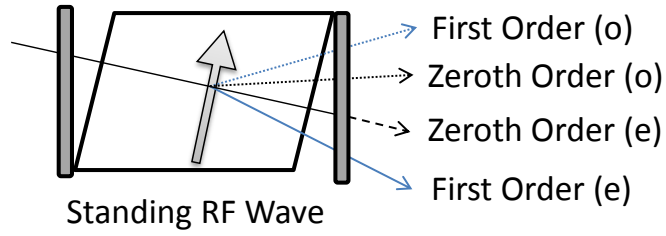


Figure 6: An AOTF undergoing Bragg diffraction with an unpolarized input with a RF wave applied represented by the arrow. Two linear polarizers are added to the system, the first linear polarizer removes the ordinary polarization removing the outputs with the dotted lines and the second linear polarizer removes undiffracted extraordinary light shown by the dashed line.

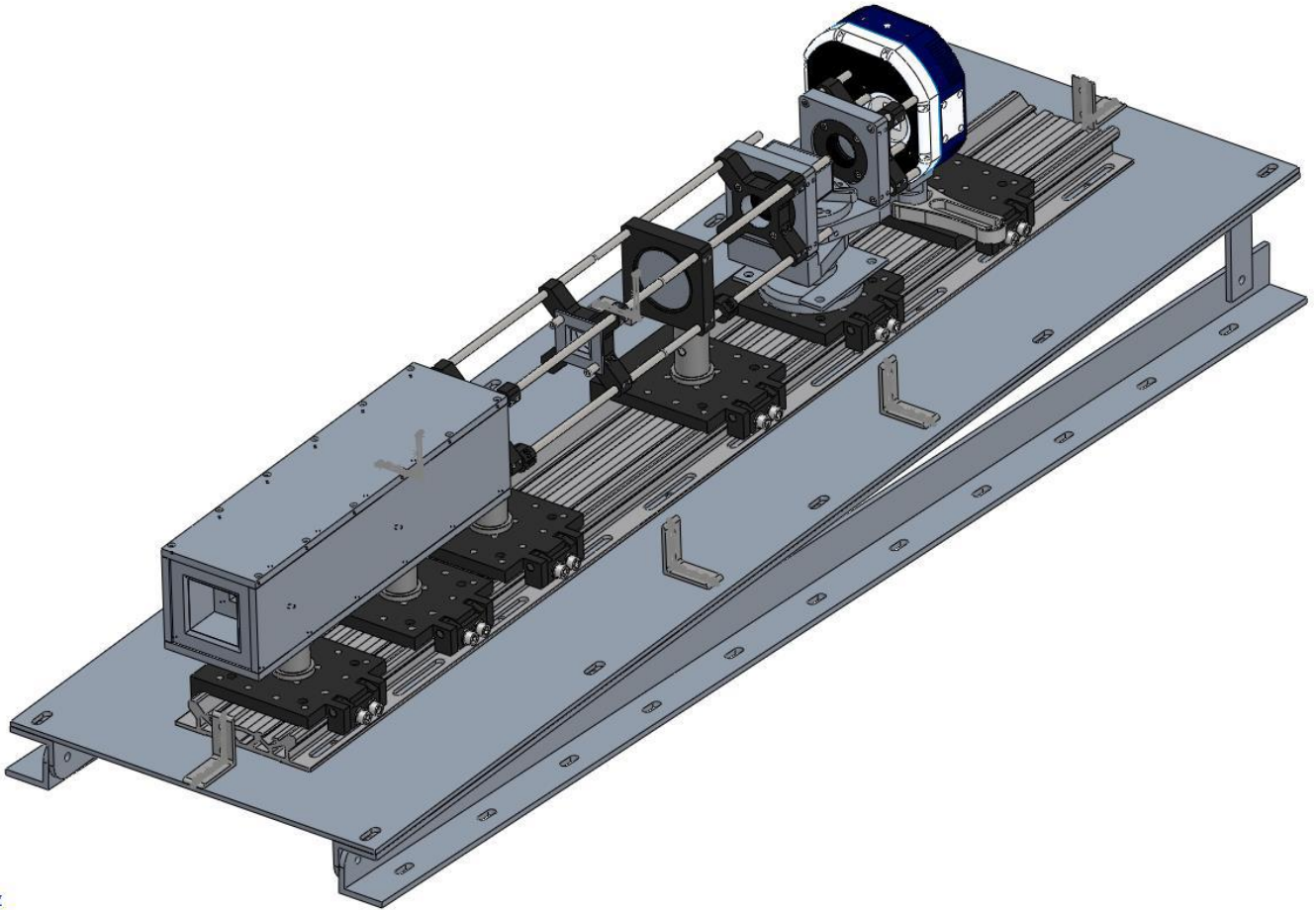


Figure 7: An isometric view of the complete ALI system with the baffle and 3° slant required to correctly position the field of view. Light tight case absent from diagram.

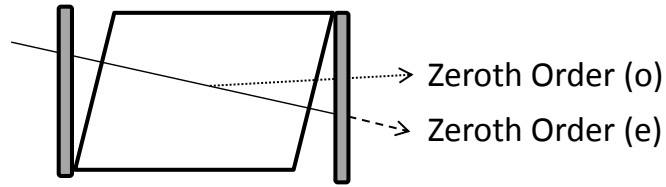


Figure 8: An AOTF with the RF disabled so no Bragg diffraction is occurring and the input is unpolarized. Two linear polarizers are added to the system, the first linear polarizer removes the ordinary polarization removing the outputs with the dotted line and the second linear polarizer removes undiffracted extraordinary light shown by the dashed line. However the polarizers are not 100% efficient and some light propagates through the system.

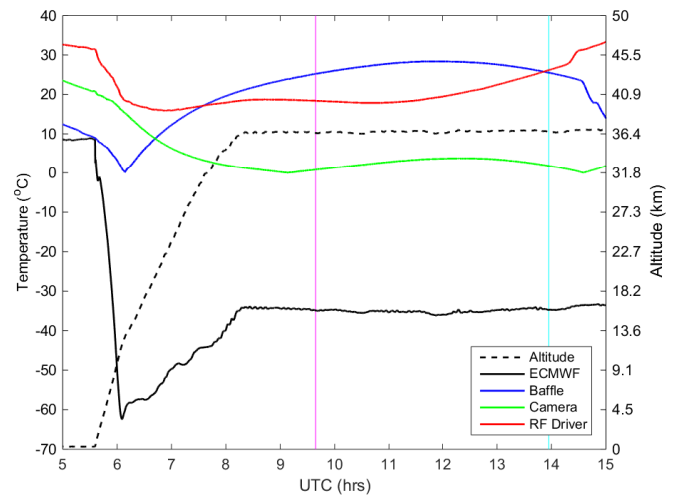
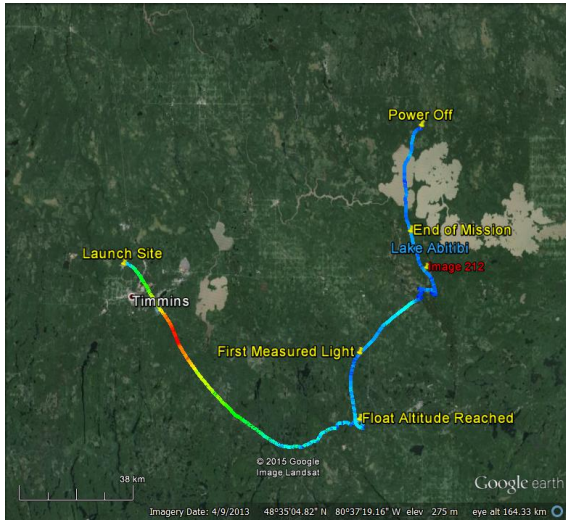


Figure 9: (A) The GPS data from ALI during the Nimbus 7 mission generated via Google Earth. The colour of the line represents the absolute speed of the gondola during the mission. Important landmarks are noted on the image. The end of mission represent the end of the aerosol mission. No GPS data was collected from ALI after power down. The location of image 212 is the red label. (B) The temperature and altitude profiles from the NIMBUS 7 flight. The time of image 212 is shown by the cyan vertical line and first light measured by ALI occurs at the magenta vertical line.

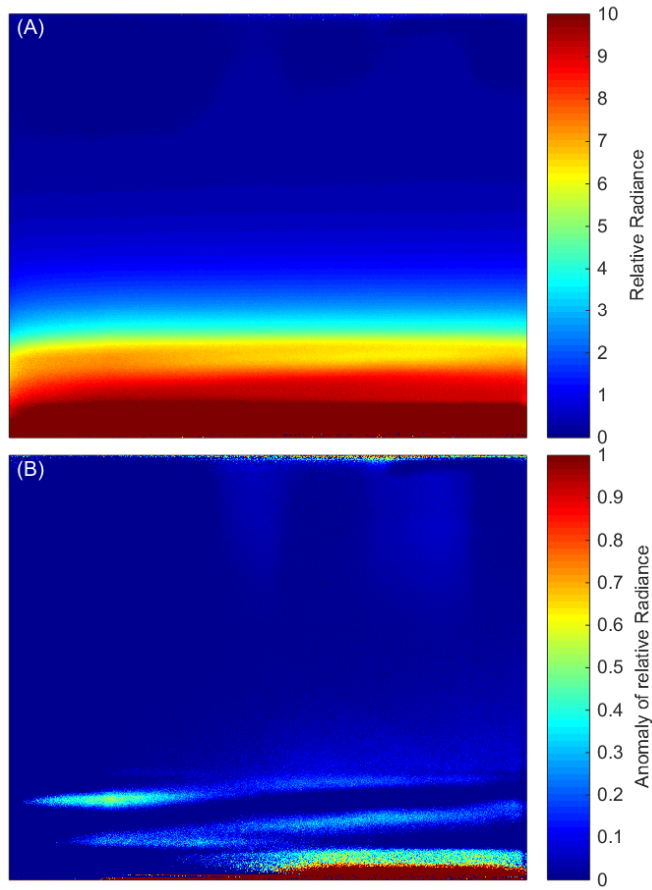


Figure 10: (A) Final calibrated 750 nm image, taken at 13:57 UTC located at 48.55°N, 80.00°W with a solar zenith angle and solar scattering angle of 63° and 98°. (B) The same 750 nm image with the mean of the profile removed from the image leaving the residual signal that shows thin clouds.

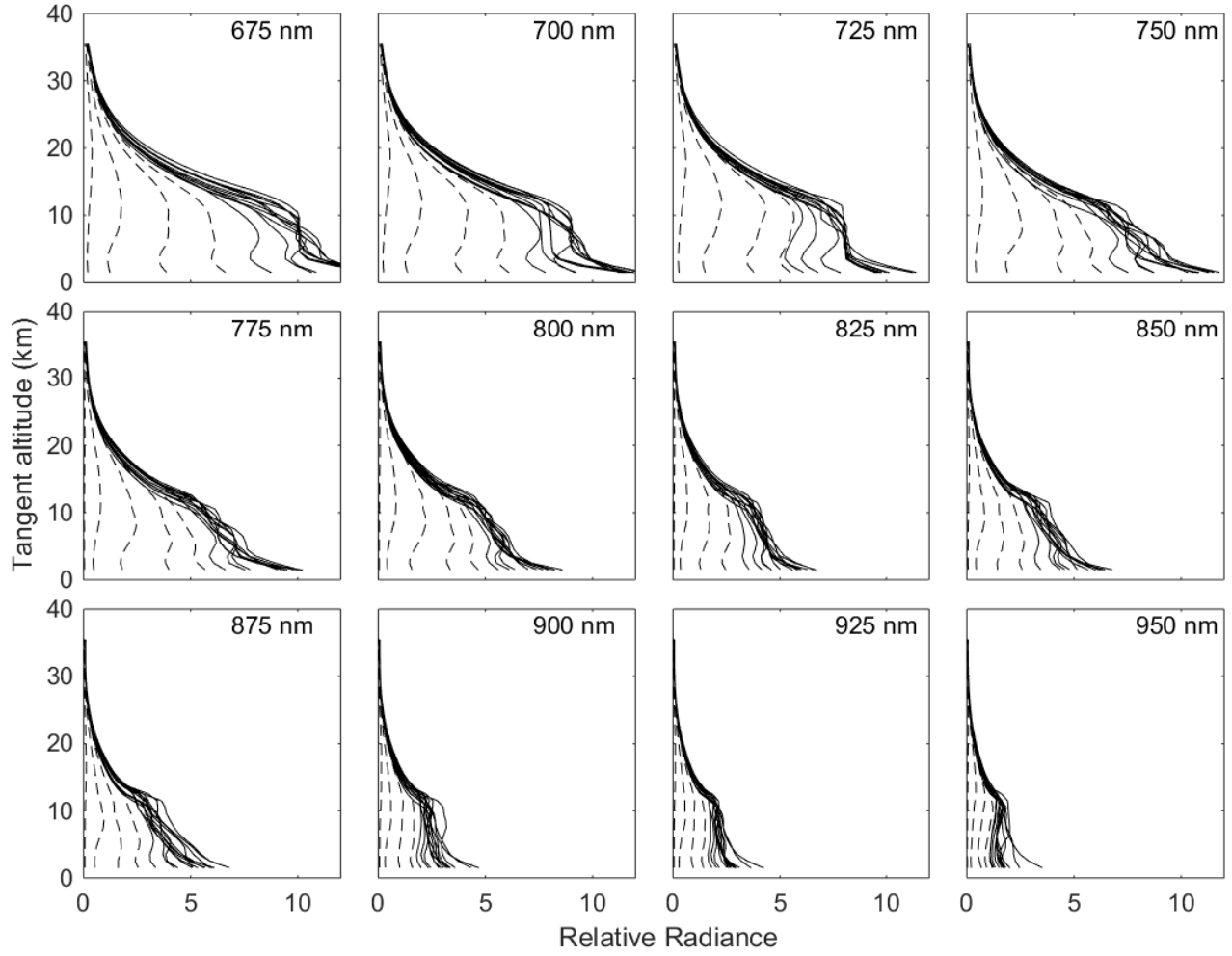


Figure 11: ALI relative radiance vectors from 12 of the 13 wavelengths from the NIMBUS-7 flight in which the center 25 pixels horizontally have been averaged to create a vertical profile and averaged to 1 km vertical resolution. Each panel presents the radiance vectors from a different wavelength measured which is denoted in the top right corner. The dashed lines are radiance profiles where the solar zenith angle is greater than 90° and solid lines are profile where the solar zenith angle is less than 90° .

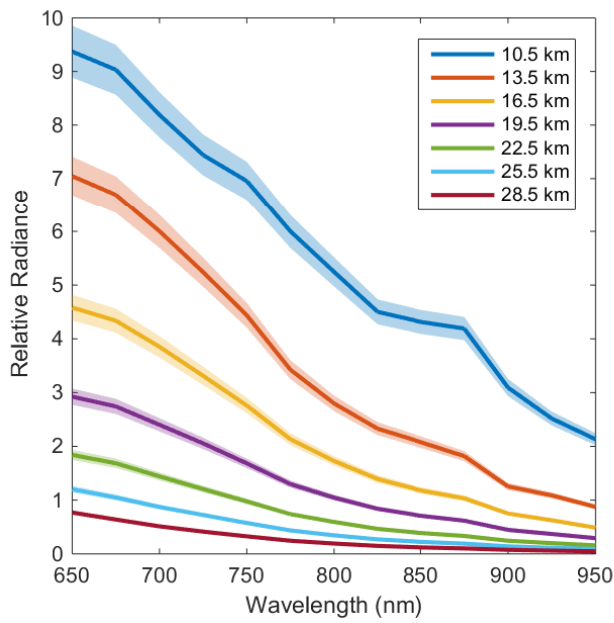


Figure 12: Level 1 relative radiances spectrally from 650 nm to 950 nm as measured from ALI at approximately 14:20 UTC consisting of images number 204 to 216 looking 90° in the azimuth from the sun facing southwards. These spectral profiles are presented at several tangent altitudes with a horizontal look direction of 0° . The shading represents the error on the radiances.

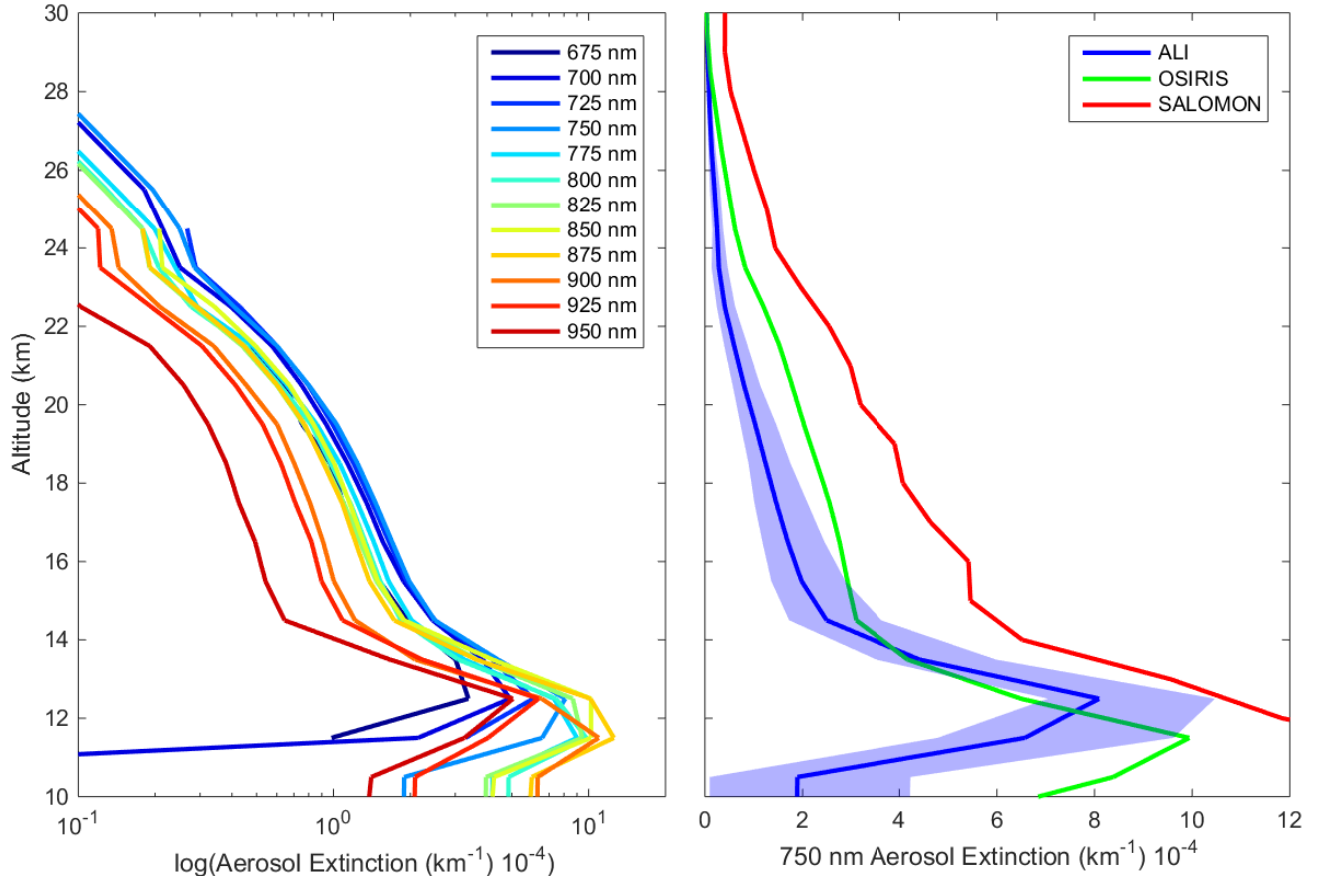


Figure 13: Left is the retrieved aerosol extinction profiles from the last complete imaging cycle consisting of images 205 to 216 from the 0.0° horizontal line of sight. Right is the 750 nm ALI aerosol extinction in blue with its error represented by the shading compared to the 750 nm extinction measured by OSIRIS and SALOMON in green and red respectively.

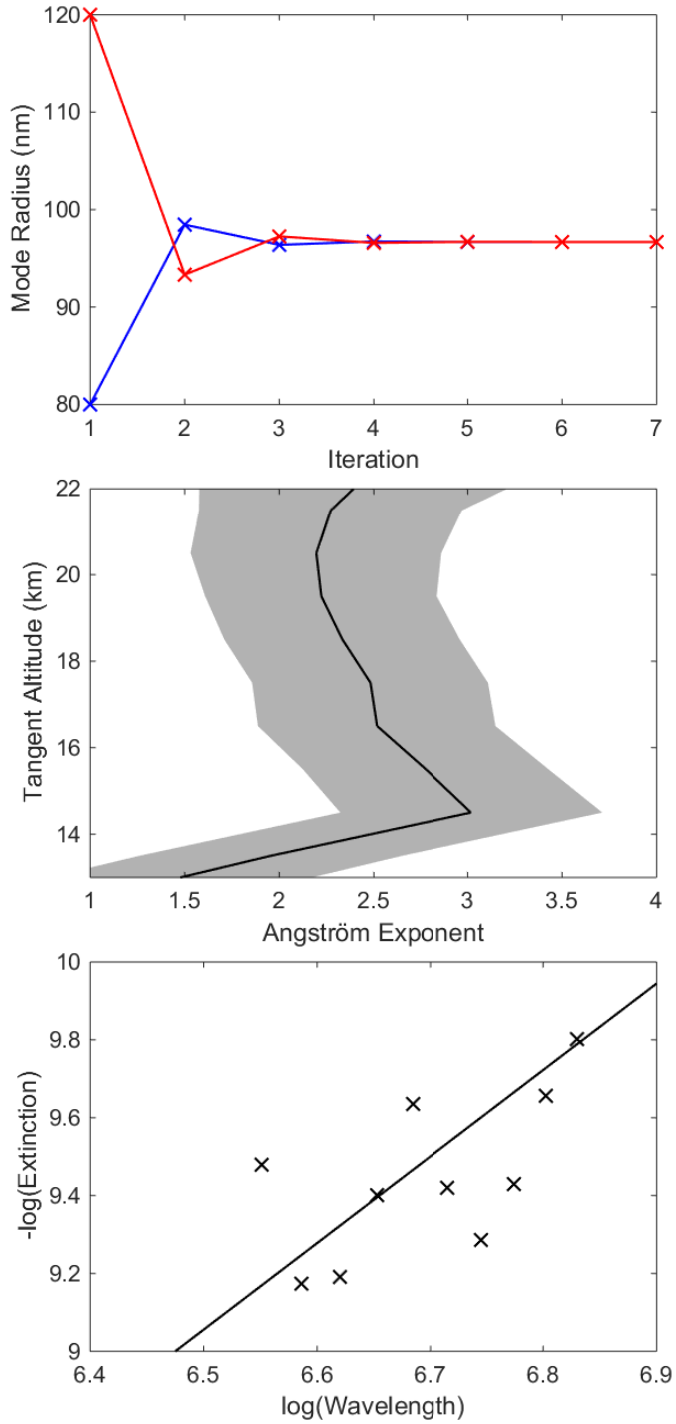


Figure 14: The top panel shows the convergence of two sample particle size retrievals over the iterations, blue and red represent an initial state of 0.08 and 0.12 μm respectively. Both initial states converge to the same value over approximately 4 iterations in the particle size retrieval method. The second panel is the final Angström exponents determined for images 204-216, the final measurement cycle, during the Timmins 2014 campaign and the shading represents the error associated with the least squares fit. The last panel shows a typical least squares fit of the retrieved extinction values over wavelength to determine the Angström exponent at model altitude of 20.5 km.